



Repositorio Institucional de la Universidad Autónoma de Madrid

<https://repositorio.uam.es>

Esta es la **versión de autor** del artículo publicado en:

This is an **author produced version** of a paper published in:

Nanotechnology 26.11 (2015): 115502

DOI: <http://dx.doi.org/10.1088/0957-4484/26/11/115502>

Copyright: © 2015 IOP Publishing Ltd

El acceso a la versión del editor puede requerir la suscripción del recurso

Access to the published version may require subscription

Continuous-flow system and monitoring tools for the dielectrophoretic integration of nanowires in light sensor arrays

A. García Marín,^{1,*} C. García Núñez,¹ P. Rodríguez,¹ G. Shen,² S. M. Kim,² P. Kung,² J. Piqueras,¹ J. L. Pau¹

¹Grupo de Electrónica y Semiconductores, Departamento de Física Aplicada, Universidad Autónoma de Madrid, Cantoblanco, 28049 Madrid, Spain

²Department of Electrical and Computer Engineering, the University of Alabama, AL 35487, USA.

*E-mail address: antonio.garciamarin@uam.es

Abstract. Although nanowires (NWs) may improve the performance of many optoelectronic devices such as light emitters and photodetectors, the massive commercialization of these devices is limited by the difficult task of finding reliable and reproducible methods to integrate the NWs on foreign substrates. This work shows the fabrication of zinc oxide (ZnO) NWs photodetectors on conventional glass using transparent conductive electrodes to effectively integrate the NWs at specific locations by dielectrophoresis (DEP). The paper describes the careful preparation of NW dispersions by sedimentation and the dielectrophoretic alignment of NWs in a home-made system. This system includes an impedance technique for the assessment of the alignment quality in real time. Following this procedure, ultraviolet photodetectors based on the electrical contacts formed by the DEP process on the transparent electrodes are fabricated. This cost-effective mean of contacting NWs enables front- and back-illumination operation modes, the latter eliminating shadowing effects caused by the deposition of metals. The electro-optical characterization of the

devices shows uniform responsivities in the order of 10^6 A/W below 390 nm under both modes, as well as, time responses of a few seconds.

Keywords: transparent conducting oxides, dielectrophoresis, sedimentation, ZnO nanowires, UV photodetectors.

1. Introduction

Nanowires (NWs) are promising candidates to form part of near-future electronic and optoelectronic devices due to suitable properties such as their high crystal quality and their tunable optical absorption, which are expected to foster the improvement of sensitivity of actual thin film based technology through the enhancement of the surface-to-volume ratio [1-2]. These one-dimensional structures can be developed in many material technologies such as carbon-based materials, metal oxides, IV-group semiconductors, III-V semiconductor compounds and noble metals [3-4]. In metal oxide materials, zinc oxide (ZnO) NWs are fascinating structures due to their remarkable optical, electrical and piezoelectric properties [5]. The abundance of Zn in the nature compared to other metals and the simplicity of the methods commonly used to grow ZnO based NWs, allow their cost-effective implementation in many applications such as ultraviolet (UV) and white lightning [6], gas and biological sensing [7-10], energy piezogeneration [11], photovoltaics [12] and UV photodetection [13-16].

In UV light sensing, ZnO NWs (energy bandgap, $E_g=3.3$ eV) show some of the highest photoconductive gain values among all the wide bandgap nanostructured semiconductor compounds with high UV absorbance. The mechanism is based on the photogeneration of electron-hole pairs when the radiation is absorbed in the ZnO NW and the recombination of photo-generated holes through the occupied surface states. This recombination provokes the desorption of O_2 molecules from the NW surface releasing surface trapped electrons to the NW volume,

increasing the amount of free carriers, and hence, the conductivity. In addition, the surface recombination of holes increases the relaxation time of photo-generated electrons, which also contributes to enhance the photoconductive gain. Different methods have been proposed in order to improve the slow response speed of ZnO NW devices, including the fabrication of rectifying Schottky barrier contacts [17], p-n heterojunctions or metal oxide semiconductor barriers [18].

One important issue which reduces the large scale commercialization of highly integrated NW-based devices is the fast and reliable manipulation of those nanostructures on small areas. Different approaches are under investigation, such as dielectrophoresis (DEP) [19-21], magnetophoresis [22], Langmuir-Blodgett [23], bubble blowing [24], contact printing [25-26], and nanoscale combing [27]. DEP has been successfully proved to be a cost-effective method to trap and also to align nanoparticles [28], NWs [21, 29-30] and carbon-based nanostructures [31-33] between electrodes, as well as, to separate different particles [34] and cells [35-36] in microfluidic systems. Briefly, this technique relies on alternating current (AC) electric fields to align those nanostructures at specific sites through the polarizability of dielectric structures [37]. Most of earlier reports on DEP integration of NWs rely on drop-casting methods on coplanar electrodes. However, drop-casting DEP limits the reproducibility of the technique and produces final surfaces contaminated with unaligned NWs that sediment by gravity action before reaching the assembling site. Continuous flow system in microfluidic cells reduce significantly surface contamination, enabling the use of monitoring techniques, the implementation of specific bias recipes to control accurately the trapping kinetics, and the possibility of mixing materials in the same solution which can be independently trapped in several locations across the wafer changing the signal parameters (heterogeneous DEP). All these advantages make the use of continuous flow systems attractive for automating production processes in industrial environments.

On the other hand, a method to monitor NW assembly in real-time during the DEP process is desirable to improve the control over the number of aligned NWs as a function of time. This can provide information about the evolution of the process whose efficiency to trap NWs can change over time due to the modification of the inter-electrode potential. Furthermore, although

several studies have been performed to evaluate the effects of AC voltage and frequency on the DEP alignment, it is a challenge to control the trapping rate only through those parameters because of local variations of the NW concentration over the alignment sites. In addition, large voltages can induce solvent electrolysis whose effects are bubble formation and electrode degradation [38-39]. Real-time monitoring can help to detect those anomalies as soon as they happen, allowing fast correction of the alignment parameters. The few works that address this point in the literature focus on the use of impedance monitoring. In highly conductive carbon nanotubes, it is found that the variations of the impedance are dominated by changes in the parallel resistance [40].

In this work, we provide insight on those matters by integrating ZnO NWs on transparent substrates by DEP for the fabrication of UV photodetectors. ZnO NWs are transferred to a liquid medium by sonicating the as-grown sample. To enhance the NW concentration and get rid of possible impurities, a sedimentation step is followed prior to the DEP process. A calibration curve is performed to estimate the NW concentration in further experiments by using transmittance monitoring. NWs are in-parallel integrated in linear arrays of assembling sites defined on glass substrates from a home-made DEP system. The DEP electrodes are made of a transparent conducting oxide giving rise to chips with fully transparent characteristics. We also investigate the continuous monitoring of NW assembly through the changes in parallel resistance. The uniformity, speed, and spectral responsivity are measured in the fabricated sensors. Transparency of substrate and electrodes allows the device operation under front- and back-illumination, a useful property for flip-chip bonding integration.

2. Experimental details

2.1. Chemicals

The dispersions are prepared with ultrapure deionized H₂O (18 MΩ·cm) obtained from an Ultramatic Wasserlab purification system or with ethanol (EtOH) obtained from Panreac (Spain).

2.2. ZnO NW solution preparation

ZnO NWs are grown by vapor phase transport at high temperatures ($T > 750^{\circ}\text{C}$) in a Tempress furnace on Si(100) and sapphire c-plane (0001) substrates, as thoroughly described elsewhere [41-42]. To integrate the NWs in the proposed sensors, the nanostructures are separated from the substrate by sonication and dispersed in a liquid medium. After drying out, the NW powder is weighed and immersed in EtOH or H_2O and further sonicated for times between 30 and 180 s. Resultant concentrations out of this process range from 80 to 380 mg/L. A purification step is followed in order to get rid of large ZnO clusters which may impact negatively on the DEP process by short-circuiting the electrodes. This step is carried out by leaving the dispersion motionless during 1 h. During that time, larger particles sediment faster whereas smaller NWs remain more homogeneously distributed in the medium. Eventually, the purified supernatant is transferred to another container and heated up in order to increase the concentration by solvent evaporation.

2.3. Dispersion characterization by spectrophotometry

Optical properties of NW dispersions are studied by using a double beam UV/Cary 100 spectrophotometer. All measurements are performed using 1 cm path length quartz cuvettes. Every absorbance (*Abs*) spectrum is referenced to a blank sample containing pure solvent.

Spectra are recorded in the 360-420 nm wavelength range at 1 nm step. Optical extinction in that spectral range is governed by scattering and also includes part of the absorption range of the NWs above the ZnO bandgap. To study sedimentation processes, kinetic measurements are performed at a constant wavelength of 400 nm for a time span of 1 h. At that wavelength, *Abs* variations can be mainly attributed to NW scattering. By measuring *Abs* in dispersions with different NW concentrations and counting the number of NWs, a calibration curve is obtained to determine NW concentrations in unknown samples. In this curve, concentration errors (horizontal bars) are estimated as the standard deviation in the counting process of the number of NWs in 1

μL taken from the middle of the cuvette for the different dispersions, and drop-casted on a Si substrate. Absorbance error (vertical bars) are estimated from 3 measurements for each sample.

As the NW concentration in the flow circuit of the DEP system is found to change slightly along the circuit as a result of trapping, the concentration uniformity along the circuit is evaluated by optical means extracting aliquots from the inlet and outlet ports and comparing their *Abs* with that of the original dispersion.

2.4. Electrode fabrication and alignment by dielectrophoresis

For dielectrophoretic alignment of the NWs, transparent chips are prepared on glass substrates with pre-patterned transparent conductive electrodes defined by optical lithography and chemical etching. Prior to electrode deposition, substrate is cleaned to remove organic left-overs by immersing the samples in hot trichloroethylene, acetone and EtOH. Then, 300 nm thick thin films of Al-doped ZnO (AZO) ($1.1 \times 10^{-2} \Omega\text{-cm}$ Hall resistivity) are deposited by radio-frequency (rf) magnetron sputtering on those transparent substrates at 300 °C by using a 99.999% ZnO w/2% Al₂O₃ target. The final chip comprises two multi-fingered electrodes with alignment sites defined by gaps of variable widths between 4 and 8 μm.

To integrate nanostructures, the receiver substrates are assembled into a home-made DEP system. This includes a polytetrafluoroethylene cell and an O-ring where the substrate is attached. The inner diameter of the O-ring is about 5 mm containing 20 active alignment sites of the receiver substrate. Total volume of the microfluidic cell is 20 μL. NW dispersions are loaded into the syringe cartridge and pumped into the system by a peristaltic pump at a speed of 6 mL/min. The cartridge concentration during the fluid injection is monitored by measuring the transmittance of the dispersion through an optical coupler containing a 650 nm red laser and an off-axis silicon n-p-n phototransistor (Ref. BPW77N, Vashay). The output analog signal from the detector is recorded by using a microcontroller.

Prior to reach the DEP cell, nanostructures pass through a filter with 200 μm pore size to remove large size contaminants. For the present study, sinusoidal waveforms with effective

voltages (V_{rms}) between 4 and 10 V, and frequencies of 10 and 100 kHz, are applied between electrodes.

In order to monitor NW trapping through impedance measurements, an inductance-capacitance-resistance (LCR) meter is connected to the pair of electrodes on the transparent substrate by using conductive silver paint. The variation of parallel resistance is measured during the alignment and compared with those values taken in pure EtOH. By counting the aligned number of NWs by optical microscopy at the end of the process, a correlation is established between the number of NWs and the relative parallel resistance variation.

2.5. Sensor photoresponse

The electro-optical characteristics of the fabricated sensors are studied in dark and under UV/visible illumination. The sensor is connected in series with a 1.5 M Ω load resistance. This resistance is chosen to be close to that exhibited by the sensor under illumination. Voltage drop in the load resistance is recorded in real time using serial communication and stored in a microcontroller. The measured signal is transformed into photocurrent (I_{photo}) by subtracting the baseline to the output voltage and dividing by the load resistance.

In all the electro-optic experiments, the sensor is illuminated through an optical fiber using different light sources. For assessment of the response speed, the device is exposed to light pulses of a deuterium lamp (Ref. DH-2000 Deuterium Tungsten-Halogen Light Source, OceanOptics (USA)). To study the uniformity of the response across the active area, I_{photo} is also measured by scanning the assembly area using a precision micropositioner.

Spectral responsivities measurements are also carried out at different DC bias between 3 and 11 V using a Xenon lamp as the light source coupled to a 1/8 m monochromator. To exploit the transparent characteristics of the chips, back-illumination is also studied and compared with the regular front-characterization. All measurements are performed on a non-reflective surface to minimize specular reflection.

3. Results and discussion

3.1. Preparation of the NW dispersions

In order to improve the quality of the dispersion, a sedimentation process is introduced after the sonication process. The sedimentation rate of particles depends on the balance of different forces [43-44]. The net force on each particle comprises gravitational force (F_g), which is directed downwards; and buoyancy (F_b) and drag (F_d) forces, which are oriented upwards. They are defined as:

$$F_b = V \cdot \rho_m \cdot g \quad (1)$$

$$F_g = m \cdot g \quad (2)$$

$$F_d = f_0 \cdot v_t = 6 \cdot \pi \cdot \mu \cdot v_t \quad (3)$$

where m , V , g , ρ_m , ρ_{ZnO} , v_t , μ and r represent the particle mass, particle volume, gravity constant, medium and particle densities, terminal velocity, medium viscosity, and the sphere radius, respectively. The constant f_0 is known as the frictional coefficient. According to the Stokes's law, these equations (1-3) allow estimating v_t , which represents the speed of a falling sphere when the net force is zero. Thus, this parameter can be obtained from the following equation:

$$v_t = \frac{V_{sp} \cdot g \cdot (\rho_{ZnO} - \rho_m)}{f_0} \quad (4)$$

V_{sp} being the volume of the sphere. According to hydrodynamics, f_0 is dependent on the particle morphology. For the long-rod case, F_d is redefined as $F_d = f \cdot v_t$ where f becomes:

$$f = \frac{\left(\frac{2}{3}\right)^{1/3} A^{2/3}}{\ln(2 \cdot A)} \cdot f_0 \quad (5)$$

and A represents the aspect ratio between the length of the NW and its diameter. It is important to notice that f_0 is the frictional coefficient for a sphere of an equal volume. Taking into account the other two forces, F_b and F_g , v_t for NWs can be redefined as:

$$v_t = \frac{V_{NW} \cdot g \cdot (\rho_{ZnO} - \rho_m)}{f} \quad (6)$$

V_{NW} being the volume of the NW. For equal NW and sphere volumes, differences in v_t for spheres and NWs are determined by the ratio between frictional coefficients (f/f_0). This ratio is always larger than 1 and accounts for the faster sedimentation of spheres [43]. The physical origin of this is related to the lower friction of the flowing spheres in the liquid solution.

To apply this model to the prepared dispersions, an estimation of the average size of the ZnO NWs is made using scanning electron microscopy images of drop-casted NWs on a Si substrate. The dispersion under study shows average length and diameter of $14 \pm 5 \mu\text{m}$ and $190 \pm 30 \text{ nm}$, respectively. Thus, the average aspect ratio of those NWs is approximately 75 which yields an f/f_0 ratio equals to 3.3. This means that spheres with equal volume (sphere diameter = 900 nm) are expected to fall down at 3.3 times faster than NWs. For larger spheres, the velocity is even larger. As an example, spherical particles with a diameter of $2 \mu\text{m}$ will sediment 16 times faster than the NW. In Figure 1(a), we plot V_t for spherical particles (solid lines) of different diameters in H_2O and EtOH and compare with that of the average NW (dashed lines). From those graphs, it is concluded that spherical particles with diameters larger than 500 nm are expected to suffer a faster sedimentation process than the NWs. In the present work, this fact has been used to eliminate undesired particles coming out of the substrate during the sonication process (purification). In an ideal dispersion in which all the particles were spherical, 500 nm would be the critical diameter that one may expect to filter out. It is important to notice that the alternative use of membrane filters with similar porous sizes would yield very low NW concentrations in the purified dispersions caused by the accumulation of NWs in the sidewalls of the pores which may end up clogging them. Therefore, although real dispersions usually contain impurities with

random morphologies, this filtration process is seen as an effective method to remove particles up to a submicron level while keeping large NW concentrations available for DEP processes.

Despite the different physical properties of EtOH and H₂O, i.e. viscosity and density, Figure 1(a) shows that both solvents give rise to similar terminal velocities. However, in practice, NWs can show very different velocities in both solvents due to the surface interactions among them. For the sake of comparison, ZnO NW dispersions are prepared in EtOH and H₂O solvents as described in the Experimental Procedure. To compare the sedimentation rates, an aliquot of each dispersion is introduced in quartz cuvettes, monitoring changes in the *Abs* for 1 h in a UV/visible spectrophotometer at a constant wavelength of 400 nm. Figure 1(b) represents different kinetic curves after baseline subtraction (EtOH or H₂O) for dispersions with different concentrations ranging from 80 to 380 mg/L. As expected, the measured *Abs* increases with concentration due to the increasing number of scattering centers. Interestingly, the initial values show larger *Abs* in EtOH than in H₂O, even at the first data points. It is hypothesized that this happens as a result of the stronger interaction between NWs in H₂O which tend to form larger aggregates and sediment faster than in EtOH. In both solvents, the time-dependent absorbance curves can be optimally fitted with bi-exponential functions indicating the presence of structures inside the dispersion with different characteristic sizes. The shorter time constant ranges from 210 to 420 s and is related to the sedimentation of the largest particles, either particles coming from the nucleation layer in the substrate or NW aggregates formed during the dispersion preparation. The longer time constant of the fitting is attributed to the sedimentation of dispersed single NWs and ranges from 1300 to 4000 s. In EtOH, the constants do not present a characteristic trend as a function of NW concentration. In contrast, in H₂O, the constants reduce notoriously with the increasing concentration, which also corroborates the strong interaction of NWs in aqueous media.

From the analysis of the absorbance at the end of the 1 h process, it is found that the concentration of NWs in EtOH is higher than in H₂O. As the concentration increases the trapping probability in the DEP process, the NW integration is only performed on dispersions prepared from EtOH solvent. Besides, the final NW concentrations are quite stable over the time needed

to perform the DEP alignment, 1 min, ensuring the homogeneity of the NW distribution in the solvent during the whole DEP process.

The spectral characteristic of the optical transmittances ($T\%$) is analyzed using a UV/visible spectrophotometer. A fast scan (300 nm/min) from 420 to 360 nm is performed in a NW/EtOH dispersion with a ZnO concentration of 380 mg/L. As shown in Figure 1(c), $T\%$ presents a fairly constant value around 27% above the bandgap wavelength of ZnO ($\lambda = 380$ nm), as a result of the optical losses caused by scattering phenomena. Below that wavelength, ZnO absorption contributes to reduce the $T\%$ down to 25.5%, a loss that is significantly smaller than those caused by scattering. Thus, both UV and visible light extinctions seem to be dominated by the scattering phenomena, a point that it is also confirmed by analyzing dispersions with different concentrations.

After the sedimentation step described above, the supernatant is transferred to another container and heated up near the EtOH boiling point in order to evaporate part of the solvent and increase the concentration. A highly concentrated dispersion with a final Abs of 0.29 is obtained at a wavelength of 400 nm. The number of NWs within a 1 μ L volume is estimated from microscopic images to calculate the NW concentration, yielding a value of 790 NWs/ μ L. Successive dilutions of this concentrated dispersion are performed and characterized over 1 h (Figure 1(d)). Those absorbance curves are smoother than in the as-sonicated case and do not present the fast sedimentation component thanks to the effective removal of the largest particles. Figure 1(e) shows microscopy images of 1 μ L aliquots taken from the middle of the cuvette and drop-casted on a Si substrate. An estimation of the number of NWs in the 1 μ L volume is represented as a function of absorbance (Figure 1(f)). This counting process is repeated three times for each sample in order to reduce the statistical error in the number of NWs. The calibration curve obtained from those experimental data follows a linear relationship between Abs and concentration with a coefficient of determination (R^2) of 0.9985. This behavior follows the Lambert-Beer's law which predicts that Abs is equal to $\sigma \cdot c \cdot l$ where σ , c and l are the extinction cross-section, the NW concentration, and the optical path length (1 cm), respectively [45]. From

the slope of the linear fitting, a σ value of $3.26 \times 10^{-4} \mu\text{L} \cdot \text{NW}^{-1} \cdot \text{cm}^{-1}$ is obtained. Taking into account the average size of the NWs showed above, this σ corresponds to an absorptivity value of $12300 \text{ L} \cdot \text{mol}^{-1} \cdot \text{cm}^{-1}$. It is important to notice that, although NW absorptivity accounts for all optical losses [46], it is dominated by scattering, as explained before.

For the sake of clarity, a summary of the steps followed to prepare the NW dispersion is shown in Figure 2. Experimental conditions are also included for each step. It should be noted that those conditions may change when different sizes or different nanostructures are used.

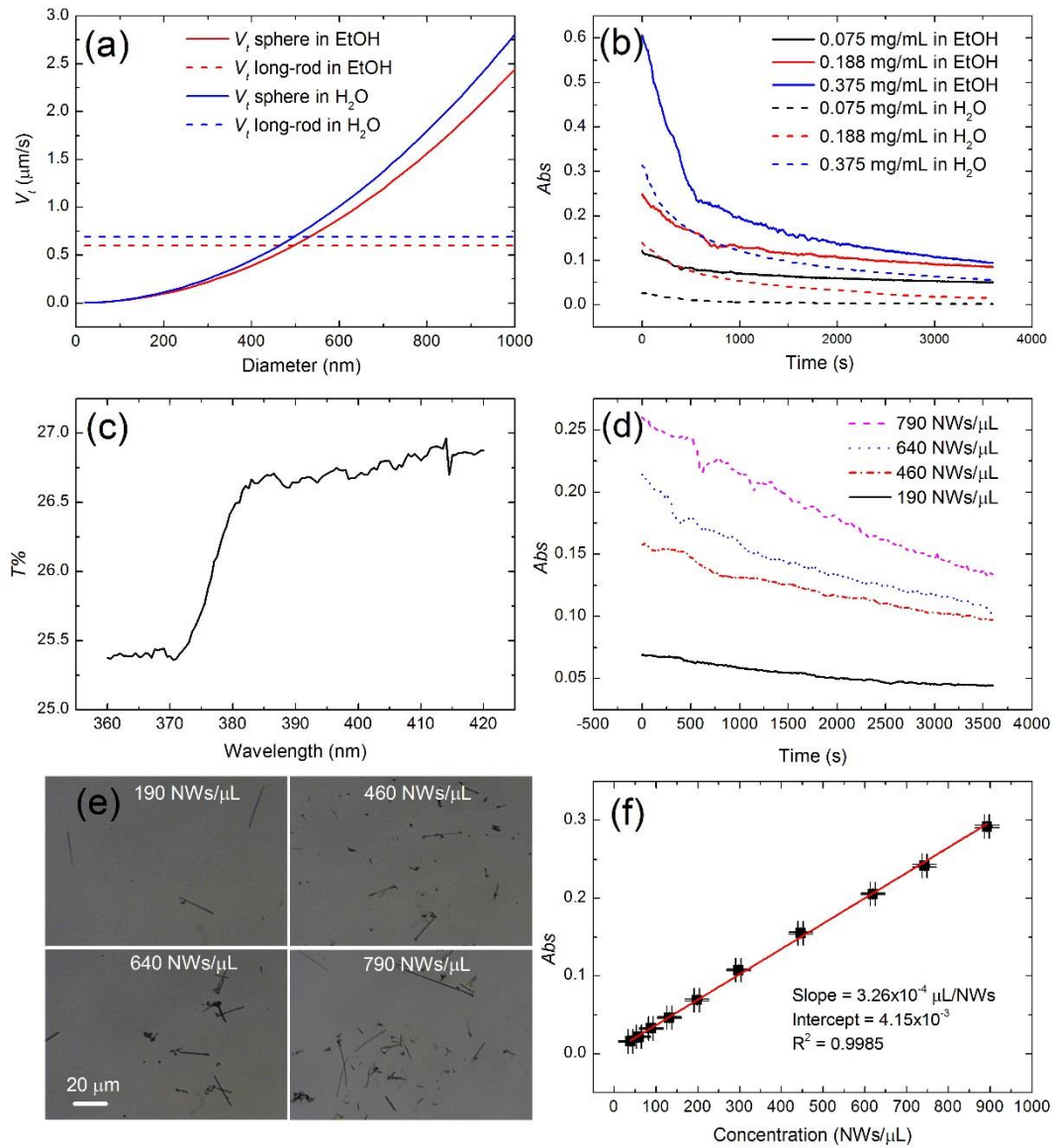


Figure 1. (a) Terminal velocities for a sphere and a long-rod ($\rho_{\text{ZnO}} = 5610 \text{ kg/m}^3$), with the same volume, in EtOH ($\rho = 790 \text{ kg/m}^3$ and $\mu = 10.7 \times 10^{-4} \text{ Pa} \cdot \text{s}$) and in H_2O ($\rho = 990 \text{ kg/m}^3$ and $\mu = 8.90 \times 10^{-4} \text{ Pa} \cdot \text{s}$); (b) kinetic measurement of the Abs as-sonicated dispersions with different concentrations between 80 and 380

mg/L for EtOH and H₂O; (c) transmission measurement of the as-sonicated ZnO dispersion in EtOH with a concentration of 380 mg/L in ZnO. The scan rate is set at 300 nm/min; (d) kinetic measurement of *Abs* in purified dispersions; (e) optical microscope images taken from the purified dispersions; (f) calibration curve obtained from different purified dispersions. Concentration error is calculated as the standard deviation obtained from three samples of the same dispersion and plotted as horizontal error bars. Vertical error bars are calculated from 3 measurements for each sample.

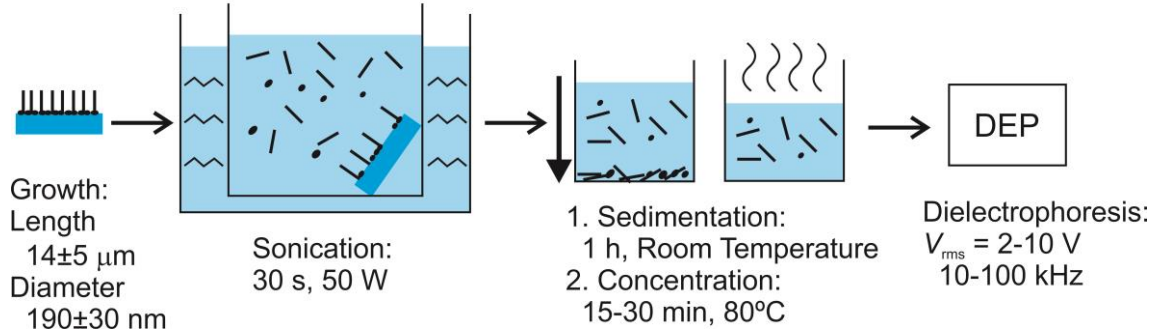


Figure 2. Step diagram of the preparation of the NW dispersions used in the DEP process.

3.2. In-situ characterization of the NW dispersion

To study the influence of the NW concentration inside the syringe cartridge during DEP, a basic optical system is developed to measure the scattered light. This system consists of a red laser diode and an off-axis phototransistor assembled around the cartridge to allow real-time measurements (see Figure 3(a)). Output analog signal is monitored by serial communication with a microcontroller board.

The syringe cartridge is initially filled with 4.5 mL of EtOH. The peristaltic pump is turned on to introduce the solvent in the system. After 2 minutes, 2 mL of EtOH are added without producing any change in the output signal. Successive 1 mL volumes of a NW dispersion (450 NWs/ μL) are added every 4 minutes. Upon NW dispersion casting, there is a fast signal increase due to the larger amount of scattered light impinging onto the detector (Figure 3(b)). After reaching a peak value, the signal decreases as the NWs disperse homogeneously inside the solvent producing a plateau in the output signal after 100s. At the end of the experiment, the plateau level

increases as new drops are casted and the NW concentration becomes larger. After 4 NW drops, the estimated NW concentration in the dispersion is about 170 NWs/ μ L.

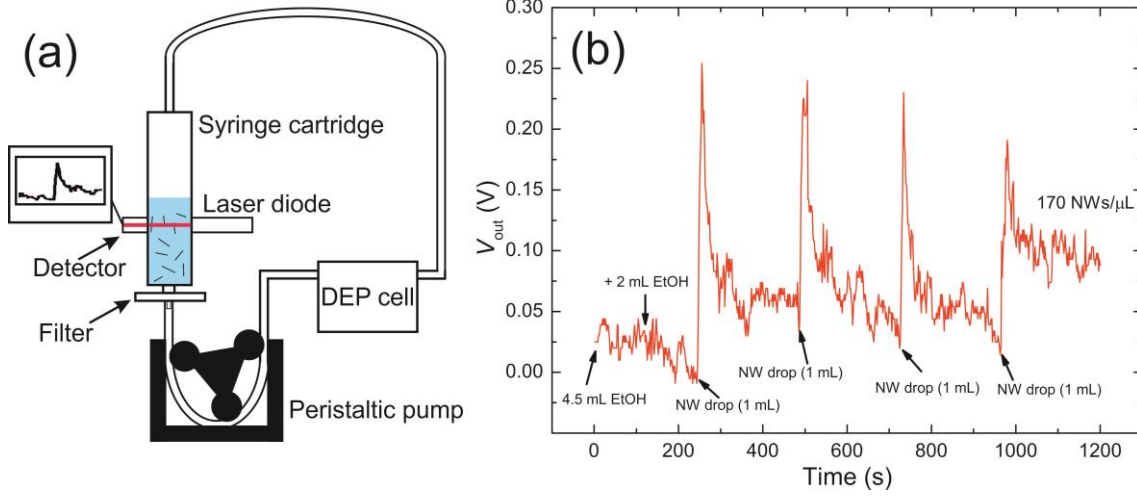


Figure 3: (a) Scheme of the optical setup used for the characterization of ZnO NW dispersions in the DEP system; (b) Analog signal obtained during the drop by drop increase of the ZnO NW concentration in the syringe cartridge.

To estimate NW losses in the whole system, the optical characteristics of the input and the output dispersions are compared in the absence of DEP bias. A 5 mL volume of a NW dispersion with a 450 NWs/ μ L concentration is loaded in the syringe cartridge and pumped into the system. Several aliquots of the fluid are extracted from different parts of the system and their absorbance measured in the spectrophotometer. Table 1 includes the concentration of NWs in those aliquots, exhibiting a reduction in the number of NWs as the dispersion flows through the system. The 200- μ m pore size filter placed at the output of the syringe cartridge blocks 28% of the NWs. After the DEP cell, the concentration measured in a single run is about 219 NWs/ μ L, i.e. a 49% of the original concentration. A rinsing step using a 2 mL volume of pure EtOH allows extracting 16% of the NWs, trapped in the system during the first run. Successive rinsing steps release 3% and 0%, respectively. The total amount of NWs that make all the way to the outlet is about 68% of the original concentration that, along with the 28% blocked in the filter, produced a total

percentage of 96%, near the total of the original concentration. The 4% uncertainty is believed to be caused by the error accumulation in the concentration estimations.

Table 1: Summary of the absorbance measurements in the DEP system (first column) and estimation of the corresponding NW losses from calibration curve in Figure 1(d) (second column). First row includes the original absorbance prior to cartridge load. Second and third rows provide data obtained before and after the DEP cell, respectively. The last three rows show values taken after successive rinsing steps (R.S.).

	Abs	Conc. (NWs/ μ L)	%
Original	0.155	450	
Before DEP cell	0.114	330	72
After DEP cell	0.078	220	49
1st R. S.	0.027	70	16
2nd R. S.	0.005	10	3
3rd R. S.	0.002	-	-

3.3. Parallel resistance monitoring

The devices are fabricated using glass substrates with evaporated AZO electrodes prepared by optical lithography and chemical etching, as described in the Experimental procedure. The electrodes present a transmittance value larger than 80% in the full visible range and give a transparent look to the receiver substrate.

After mounting those substrates in the DEP cell and performing a typical alignment process at a frequency of 100 kHz and an effective voltage (V_{rms}) of 6 V, a microscopic analysis of the surface reveals the assembled ZnO NWs on the patterned sites near the center of the cell. The low specific area of the assembling sites, which typically ranges from 8 to 30 μm^2 , preserves the high transparency to the naked eye of the final sensors, as shown in Figure 4(a). The number of trapped NWs depends on the DEP parameters and can be adjusted changing the bias voltage and/or the

frequency in a wide range from a dense coverage (Figure 4(b), left) to a sparse coverage with a few NWs (Figure 4(b), right).

To investigate the use of the inter-electrode resistance as a monitoring tool, sinusoidal waveforms with V_{rms} between 4 and 10 V, and frequencies of 10 and 100 kHz, are applied between electrodes to generate the DEP signal from the AC bias voltage supplied by an LCR meter. This instrument also allows measuring the impedance parameters of the device as the NW alignment takes place (Figure 4(c)). The electrical model used in the setup is shown in the inset of Figure 4(d). As the resistance of the electrodes is much lower than the resistance of the NWs, the variations of the parallel resistance are governed by the number of NWs trapped in the assembling sites. On the contrary, the parallel capacitance presents quite stable values during the experiments due to the high parasitic capacitance of the electrodes (~ 10 pF) in comparison to the typical NW capacitance. The electrode capacitance is caused by their large area ($2-3 \text{ cm}^2$) and it is difficult to minimize in the present setup.

The parallel resistance variations are studied during the DEP process at increasing bias voltages to find out the threshold voltage at which NW trapping occurs. Starting at 4 V, the V_{rms} is increased 2 V every 30 s, while the relative changes of the parallel resistance are monitored. These relative changes are quantified by using:

$$R_{p,r}(\%) = (R_p - R_{p,o}) \cdot 100 / R_{p,o} \quad (7)$$

where $R_{p,o}$ is the parallel resistance at the beginning of the scan and R_p is the parallel resistance measured in real time. The experiment is also performed in pure EtOH, allowing the extraction of another $R_{p,r}$ curve for comparison purposes. As can be seen in Figure 4(c), $R_{p,r}$ presents a sudden reduction every time V_{rms} is increased either under pure EtOH or NW dispersion flow. The reduction in parallel resistance is attributed to the finite exchange current density between electrodes and solvent ruled by the electrical double-layer impedance. The super-linear relationship between the current density and the applied bias causes a reduction of the parallel resistance as the bias amplitude increases. As a result of NW trapping, the interface becomes more

inhomogeneous, diminishing the charge exchange and making the changes in parallel resistance less pronounced over time. This effect produces an effective deviation of the curve taken in the DEP process from that found in pure EtOH. This deviation can be quantified from the difference between the relative changes taken as $\Delta R_{p,r}(\%) = R_{p,r}^{NW} - R_{p,r}^{EtOH}$. The analysis of the difference at 100 kHz shows that the onset of the deviation begins at 6 V, matching the minimum amplitude needed for NW trapping in the setup. On the other hand, the increasing difference between both curves with the bias voltage is the result of the assembly of a larger amount of NWs. Careful examination of the trapping sites after processes run at a constant AC bias confirms this point, corroborating the adequateness of the method to identify NW deposition in the DEP cell. Figure 4(d) presents $\Delta R_{p,r}$ as a function of the bias voltage, along with the number of NWs trapped in the alignment sites and estimated from the microscopic analysis.

Furthermore, the larger amplitude of the steps as the bias voltage increases indicates that the monitoring method is more sensitive to NW trapping at 100 kHz than at 10 kHz. The reason is that, at lower frequencies, the exchange current density is screened by the ion rearrangement in the electrical double layer causing smaller changes in the parallel resistance. In each half of the cycle of the applied potential the double layer has enough time to be built, giving rise to a potential drop. On the contrary, at higher frequencies, the double layer has less time to form since the mobility and diffusion of ions in the solution has a finite value. This reduction of the ion screening effect at higher frequencies produces a better scenario to measure the changes caused by the NW trapping [47].

Despite the screening effect and the lower number of trapped NWs, the 10 kHz curves also present a lower parallel resistance reduction in the presence of NWs. Interestingly, an unexpected resistance drop is observed at a 10 V bias. To find out its origin, a pure EtOH droplet is drop-casted on the assembly area of one of the substrates while DEP bias is applied to the pair of electrodes. At those conditions, real-time optical microscopy reveals continuous bubble formation that leads to irreversible damage of the electrodes. The phenomenon is related to solvent electrolysis and hydrogen gas formation, which produce erosion and atom migration [38-39]. The

strong current increase measured between both electrodes gives rise to a significant reduction of the parallel resistance. The identification of those anomalies during the DEP process is another practical advantage of the method.

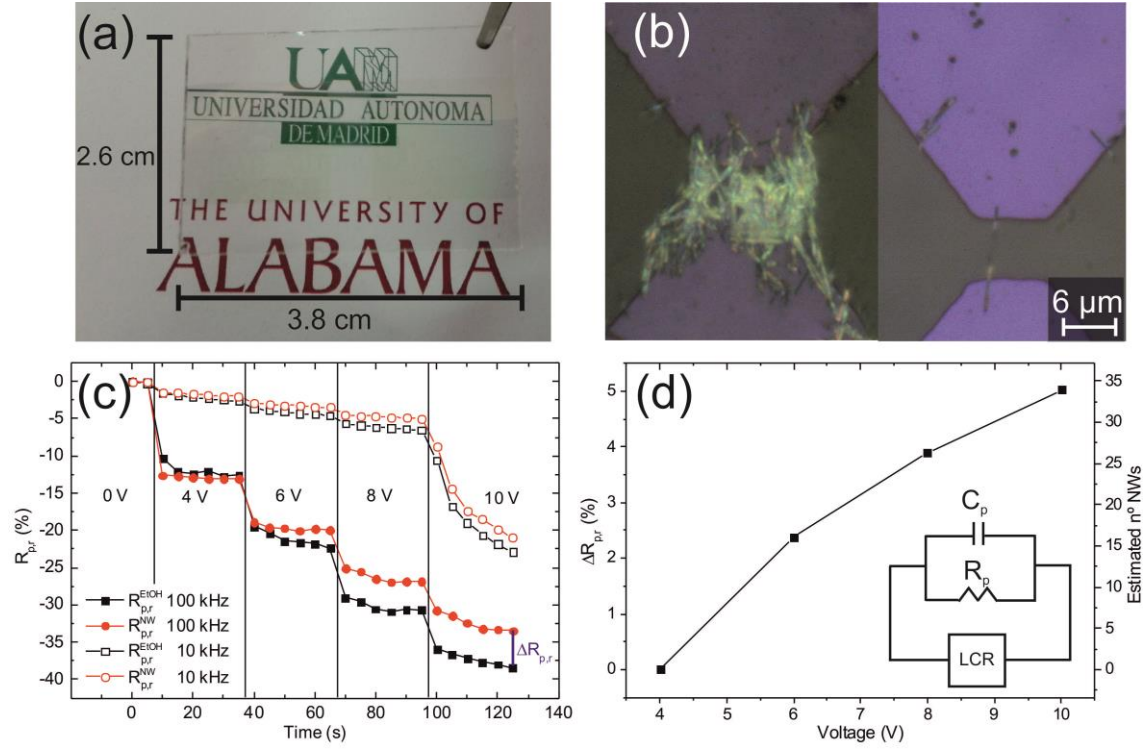


Figure 4: (a) Picture of one of the sensors including AZO electrodes and assembled NWs; (b) optical microscope images of the assembling sites after 1-minute DEP process with an estimated number of aligned NWs of 10-20 for the most covered alignment sites. Left-hand side picture shows one of the assembling sites fully covered with trapped NWs, whereas right-hand side picture exhibits a single NW trapping event on the assembly area; (c) relative changes of the parallel resistance ($R_{p,r}$) as the bias voltage is raised from 4 to 10 V at 10 (open symbols) and 100 kHz (solid symbols). The bias scan is performed in pure EtOH ($R_{p,r}^{EtOH}$, black) and in NW dispersion ($R_{p,r}^{NW}$, red); (d) $\Delta R_{p,r}(\%)$ difference measured at 100 kHz. The number of NWs aligned at every V_{rms} , and estimated through independent DEP processes, is included at the right-most y axis. The inset represents a diagram of the electrical model used to assist the understanding of the monitoring method.

3.4. Electrical characteristics and UV photoresponse

The current-voltage (I - V) characteristics of the devices are studied in dark and under UV illumination by using a semiconductor parameter analyzer after a DEP alignment process at a 100 kHz frequency and a 10 V bias voltage. The variation of the span of the DEP process under those conditions leads to a different number of NWs per pixel from a few NWs to tens of them. The dependence of the dark current as a function of the DEP time is included in Figure 5. A DEP time of 30 s allows us to integrate about 3-5 NWs per pixel yielding low dark currents with non-linear characteristics as a function of voltage. The 1 min span produces an average number of bridging NWs per pixel in the range of 10-20 and a dark current value of about 1 nA at low voltages. A 3 min span produces high dark currents in the mA range with a linear I - V characteristic and a large average number of bridging NWs per pixel (>40). The inset of this Figure 5 provides SEM pictures of the NW alignment sites under those DEP times.

For UV illumination, a deuterium lamp, coupled to an optical fiber and a lens, is used to produce a uniform power density over the active area of the device of about $1.4 \mu\text{W}/\text{cm}^2$. Under a 100 kHz and V_{rms} of 6 V (time span of 1-minute), the NWs densely cover the array of alignment sites as a result of the trapping process (estimated number of aligned NWs of 10-20 for the most covered alignment sites). The curves in Figure 6(a) show a large current increase during UV illumination under positive and negative biases. The dark current presents sub-linear dependence on the bias voltage, reaching values between 10 and 20 pA at ± 5 V. The small asymmetries found under positive and negative biases are attributed to different contact resistances between the NWs and the AZO electrodes. It is important to notice that the light curves are the result of the illumination of the NWs on the assembling sites and that selective illumination of the AZO electrodes does not produce any significant variation over the dark current.

The electro-optical characteristics are analyzed following the experimental procedure. The voltage drop in the load resistance is monitored using serial port communication with one of the

10-bit analog to digital converters in an ATmega328 microprocessor (inset of Figure 6(b)). The measured signal is transformed into photocurrent (I_{photo}) by subtracting the baseline to the output voltage and dividing by the load resistance. Light pulses from a broadband deuterium light source are applied on the alignment sites. As shown in Figure 6(b), the sensor exhibits a fast response to the UV lamp with two characteristic time constants. The fast one is related to photo-generated charges promptly swept across the space-charge-region at those NW regions in contact with the electrodes. The long component (time constant ≈ 10 s) appears as a result of the surface electron release and the consequent oxygen desorption. This mechanism is dominant in ZnO photoconductors but becomes less important as the electric field distribution intensifies in the NW contact regions. The decay time also shows a fast response after light shutdown with a small persistent effect during a few seconds (time constant ≈ 5 s) limited by the re-adsorption process of oxygen molecules.

A scan of the optical beam along the sites shows fairly symmetrical response from side to side of the assembling area (Figure 6(c)). As the optical beam is much larger than the total area, the peak signal is related to the number of covered sites. When the optical beam is centered, the whole system is illuminated and the maximum photocurrent is obtained. The variability observed at the tails of the response curve is attributed to variations in the number of bridging NWs in the successive NW alignment sites. The inset of Figure 6(c) presents four consecutive sites covered by NWs at the center of the device.

Responsivities (R_{photo}) of the sensor are calculated as a function of wavelength and bias voltage[48]:

$$R_{photo}(\lambda, V) = \frac{I_{photo}(\lambda, V)}{P(\lambda)} \quad (8)$$

where P is the absorbed power in the active areas. This parameter is estimated from the total power P_t using the following expression:

$$P(\lambda) = P_t(\lambda) \frac{A_{sensor}}{A_{beam}} \quad (9)$$

where A_{sensor} is the optical area of the sensors and A_{beam} is the area of the optical beam (radius = 3.5 mm). This way to estimate the optical power is based on the high uniformity of the optical density across the entire beam and on the assumption that the thickness of the NW patches multiplied by the absorption coefficient is much larger than one. Indeed, studies of the uniformity of the beam carried out at the output of the optical fiber reveal power fluctuations lower than 5% across the beam area. To calculate A_{sensor} , each assembling site is considered to be a rectangle of $4 \times 6 \mu\text{m}^2$ dimensions. Thus, the total area is obtained from the product of the total number of covered sites (14 in the present study) and the estimated area per site with a result of about $336 \mu\text{m}^2$.

Finally, $P_t(\lambda)$ is the optical power measured with a semiconductor photodiode placed in the equivalent position of the sample. The top graph in Figure 6(d) shows the spectral response curves taken at different voltages between 3 and 11 V. Responsivities between 10^4 and 10^6 A/W are obtained above the cut-off wavelength. The higher response of the device as the bias increases is related to the higher collection efficiency caused by a broadening of the space charge regions of the contact areas. Additionally, the larger response of the device is also associated to a relative increase of the slower component in the time response, which suggests a larger contribution of the photoconductive gain mechanism linked to the adsorption/desorption processes of oxygen molecules.

Taking advantage of the glassy substrate and the transparent characteristics of the electrodes, the sensor can work under front- and back-illumination. Both device responses are compared using the same power density and bias voltage. Spectral responsivities are shown in the bottom graph of Figure 6(d), revealing negligible differences under both configurations. This indicates that there are not significant losses in the substrate and the AZO electrodes in the measured wavelength range thanks to the use of AZO electrodes, which present a shorter absorption edge (310 nm) in comparison to ZnO. It is important to notice that bulk ZnO or GaN UV sensors rarely show this dual operation mode due to the difficulty to reach an effective collection of photogenerated charges from absorption regions near the foreign substrate. As those regions are

usually quite defective, the efficiency of the back-illuminated devices tends to be significantly lower than that reached in front-illumination operation mode.

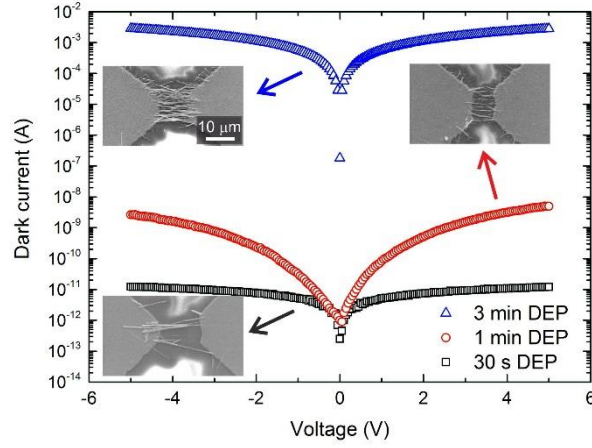


Figure 5: *I-V* characteristics exhibited by the samples in dark with NWs aligned under three different DEP times. Insets of this figure represents SEM images of the assembly sites. The magnification of the three images is the same.

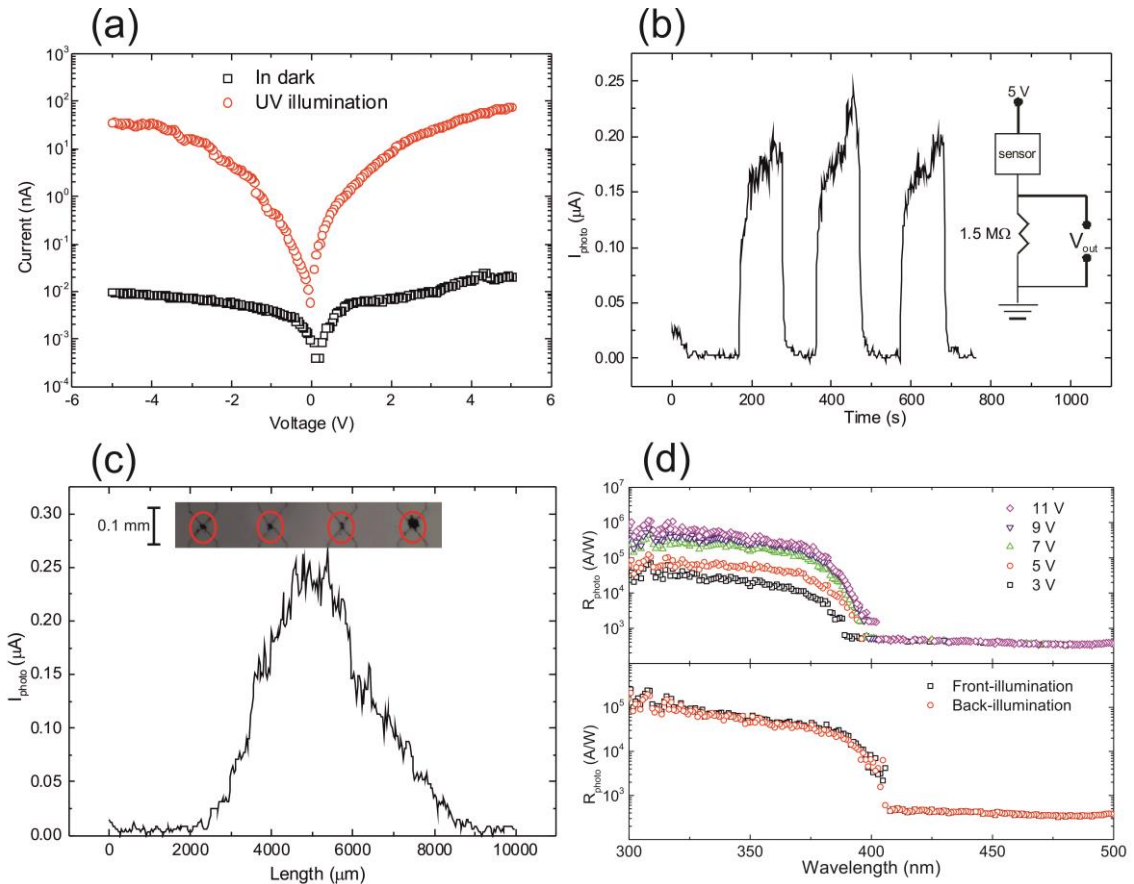


Figure 6: (a) Typical I - V characteristic exhibited by the sensors in dark and under UV illumination. (b) Photocurrents as a function of time obtained after applying light pulses with a deuterium lamp. The inset represents a scheme of the setup used to measure the photocurrent signal. (c) Photocurrent measured at different positions along the assembly line at a bias voltage of 5 V. (d) Top: estimated responsivities of the sensor at different DC voltages between 3 and 11 V. Bottom: spectral response at a 5 V bias under front- and back-illumination. The device characterized in this figure is obtained under V_{rms} of 6 V and 100 kHz (time span of 1-minute) with an estimated number of aligned NWs of 10-20 for the most covered alignment sites

4. Conclusions

ZnO NW photodetector arrays have been fabricated following a transfer process from the growth substrate to the final receptor chip using DEP. A simple sedimentation step has been proved as an effective method to remove impurities and large NW clusters that may short-circuit electrodes during DEP.

A DEP home-made system has been developed for the alignment of NWs on pre-patterned substrates. The usefulness of this system resides in the improvement of the surface quality in comparison to drop-casting methods. In addition, monitoring studies based on the parallel resistance variations between electrodes have been carried out to follow up the DEP alignment in real time. These studies have demonstrated to be helpful to estimate the number of assembled NWs and detect anomalies during the process, providing feedback for parameter optimization.

The system has been successfully used to fabricate NW-based light sensors on glassy substrates pre-coated with AZO electrodes. Taking advantage of the high visible/UV transparency of those electrodes and the high surface quality obtained after the DEP process, the devices are fully transparent and allow front- and back-illumination operation modes. The latter is a major advantage that opens the possibility of integrating the device in read-out circuits through flip-chip bonding. The same methods described here can be used in other NW technologies beyond ZnO, enabling the fast integration of those structures in electronic devices.

Acknowledgements

Authors thank E. Ruiz for their technical support. This research is partially supported by the Comunidad de Madrid (NANOAVANSENS; ref. S2013/MIT-3029), the Ministry of Science and Innovation of Spain TEC2010-20796 projects and the research funding from UAM-Banco Santander.

References

- [1] Xia Y N, Yang P D, Sun Y G, Wu Y Y, Mayers B, Gates B, Yin Y D, Kim F and Yan Y Q 2003 *Adv. Mater.* **15** 353-89
- [2] Soci C, Zhang A, Bao X Y, Kim H, Lo Y and Wang D 2010 *J. Nanosci. Nanotechnol.* **10** 1430-49
- [3] Lu W and Lieber C M 2006 *J. Phys. D: Appl. Phys.* **39** R387-R406
- [4] Baughman R H, Zakhidov A A and Heer W A d 2002 *Science* **297** 787-92
- [5] Heo Y W, Norton D P, Tien L C, Kwon Y, Kang B S, Ren F, Pearton S J and LaRoche J R 2004 *Mat. Sci. Eng. R-Rep.* **47** 1-47
- [6] Kong Y C, Yu D P, Zhang B, Fang W and Feng S Q 2001 *Appl. Phys. Lett.* **78** 407-9
- [7] Wan Q, Li Q H, Chen Y J, Wang T H, He X L, Li J P and Lin C L 2004 *Appl. Phys. Lett.* **84** 3654-6
- [8] Choi A, Kim K, Jung H-I and Lee S Y 2010 *Sens. Actuators B Chem.* **148** 577-82
- [9] Ko W, Jung N, Lee M, Yun M and Jeon S 2013 *ACS Nano* **7** 6685-90
- [10] Kang B S, Ren F, Heo Y W, Tien L C, Norton D P and Pearton S J 2005 *Appl. Phys. Lett.* **86** 112105
- [11] Wang Z L and Song J 2006 *Science* **312** 242-6
- [12] Zhang Q, Dandeneau C S, Zhou X and Cao G 2009 *Adv. Mater.* **21** 4087-108
- [13] Liu K, Sakurai M, Liao M and Aono M 2010 *J. Phys. Chem. C* **114**
- [14] Suehiro J, Nakagawa N, Hidaka S-I, Ueda M, Imasaka K, Higashihata M, Okada T and Hara M 2006 *Nanotech.* **17**
- [15] Núñez C G, Marín A G, Nanterne P, Piqueras J, Kung P and Pau J L 2013 *Nanotech.* **24** 415702
- [16] Soci C, Zhang A, Xiang B, Dayeh S A, Aplin D P R, Park J, Bao X Y, Lo Y H and Wang D 2007 *Nano. Lett.* **7** 1003-9
- [17] Zhou J, Gu Y, Hu Y, Mai W, Yeh P-H, Bao G, Sood A K, Polla D L and Wang Z L 2009 *Appl. Phys. Lett.* **94**
- [18] García Marín A, García Núñez C, Ruiz E, Piqueras J and Pau J L 2013 *Appl. Phys. Lett.* **102**
- [19] Pethig R 2010 *Biomicrofluidics* **4** 022811 1-4
- [20] Wang S, Lin Z-X, Wang W-H, Kuo C L, Hwang K C and Hong C-C 2014 *Sens. Actuators B Chem.* **194** 1-9
- [21] Raychaudhuri S, Dayeh S A, Wang D and Yu E T 2009 *Nano Lett.* **9** 2260-6
- [22] Hangarter C M and Myung N V 2005 *Chem. Mater.* **17** 1320-4
- [23] Whang D, Jin S, Wu Y and Lieber C M 2003 *Nano Lett.* **3** 1255-9
- [24] Yu G, Cao A and Lieber C M 2007 *Nature Nanotech.* **2** 372-7
- [25] Fan Z, Ho J C, Jacobson Z A, Yerushalmi R, Alley R L, Razavi H and Javey A 2008 *Nano Lett.* **8** 20-5

- [26] Yu G, Liang B, Huang H, Chen G, Liu Z, Chen D and Shen G 2013 *Nanotech.* **24** 095703
- [27] Yao J, Yan H and Lieber C M 2013 *Nature Nanotech.* **8** 329-35
- [28] Yan W, Mechau N, Hahn H and Krupke R 2010 *Nanotech.* **21** 115501
- [29] Wang D, Zhu R, Zhou Z and Ye X 2007 *Appl. Phys. Lett* **90**
- [30] Freer E M, Grachev O, Duan X, Martin S and Stumbo D P 2010 *Nat. Nanotechnol.* **5** 525-30
- [31] Duchamp M, Lee K, Dwir B, Seo J W, Kapon E, Forró L and Magrez A 2010 *ACS Nano* **4** 279-84
- [32] Blatt S, Hennrich F, Lohneysen H v, Kappes M M, Vijayaraghavan A and Krupke R 2007 *Nano Lett.* **7**
- [33] Joung D, Chunder A, Zhai L and Khondaker S I 2010 *Nanotech.* **21** 165202
- [34] Gascoyne P R C and Vykoukal J 2002 *Electrophor.* **23** 1973-83
- [35] Becker F F, Wang-Bo W, Huang Y, Pethig R, Vykoukal J and Gascoyne P R C 1995 *Proc. Natl. Acad. Sci* **92** 860-4
- [36] Voldman J 2006 *Annu. Rev. Biomed. Eng.* **8** 425-54
- [37] Pohl H A 1978 *Dielectrophoresis* (UK: Cambridge University Press)
- [38] Gencoglu A and Minerick A 2009 *Lab. Chip.* **9** 1866-73
- [39] Schwan H P 1992 *Annal. Biomed. Eng.* **20** 269-88
- [40] An L and Friedrich C R 2008 *Appl. Phys. Lett* **92**
- [41] Núñez C G, Pau J L, Ruíz E, Marín A G, García B J, Piqueras J, Shen G, Wilbert D S, Kim S M and Kung P 2014 *Thin Solid Films* **555** 42-7
- [42] Shen G, Dawahre N, Waters J, Kim S M and Kung P 2013 *J. Vac. Sci. Technol. B* **31** 041803
- [43] Holde K E v, Johson C and Ho P S 1998 *Principles of Physical Biochemistry*
- [44] Nicolosi V, Vrbancic D, Mrzel A, McCauley J, O'Flaherty S, McGuinness C, Compagnini G, Mihailovic D, Blau W J and Coleman J N 2005 *J. Phys. Chem. B* **109** 7124-33
- [45] Solé J G, Bausá L E and Jaque D 2005 *An Introduction to the Optical Spectroscopy of Inorganic Solids* (England
- [46] Pelton M and Bryant G W 2013 *Introduction to Metal-Nanoparticle Plasmonics* (EEUU
- [47] Morgan H and Green N G 2003 *AC Electrokinetics: colloids and nanoparticles: Research Studies Press Ltd.)*
- [48] Sze S M and Kwok K 2007 *Physics of Semiconductor Devices* (New Jersey: Wiley)